On the difference in material structure and fatigue properties of polyamide specimens produced by fused filament fabrication and selective laser sintering

S. Terekhina[1] · T. Tarasova[2] · S. Egorov[2] · L. Guillaumat[1] · M. L. Hattali[3]

Abstract
The present paper describes the influence of both flexure quasi-static and fatigue loading on polyamide 12 (PA12) specimens fabricated by fused filament fabrication (FFF) and selective laser sintering (SLS) processes. Rectangular prisms (ISO 178:2010) of polymer were printed and tested under sinusoidal three-point bending fatigue loading at a frequency of 5 Hz. The differences in porosity, surface roughness, and degree of crystallinity are systematically measured and linked to the mechanical fatigue properties. Fatigue analysis in the visco-elastic domain of the polymer is fully described, from fatigue behavior to energy analysis. Here, we have shown that the fatigue properties of the FFF specimens are found to be higher than those of the SLS specimens, despite their lower degree of crystallinity (more than four times). The presence of pores and their growth during fatigue tests in the sintered PA12 specimen seem to be responsible. The fatigue loss factor analysis shows that at lower stress levels, PA12 material reveals its characteristic slight visco-elastic dissipation and heating as its lifetime was exhausted. Also, the obtained results of additively manufactured PA12 were compared with those of materials obtained by injection molding (IM) and extrusion techniques. The quasi-static flexural properties of PA12 obtained by FFF and SLS processes reveal better characteristics compared to IM and extruded specimens. However, the fatigue properties of the SLS-processed polymer are 24% and 40% less than those of materials obtained by IM and extrusion.

Keywords Polyamide 12 · Fused filament fabrication · Selective laser sintering · Fatigue · Mechanical properties

1 Introduction

Additive manufacturing (AM), or 3D printing of polymeric materials, has been drawing increasing interest from industry, as well as the research and academic communities [1, 2]. Nowadays, the AM processes continue to advance from rapid prototyping methods to fabrication techniques capable of producing full-scale customized components for end-use in marketable products. As a result of these improvements, various industries such as apparel [3], biomedical [4–10], electronics [11], automotive [12], and aerospace [13] are researching this technique to produce parts. Among the different available AM techniques such as stereolithography (SL), 3D printing (3DP), digital light processing (DLP), Polyjet, or laminated object manufacturing (LOM), to mention just a few, the fused filament fabrication (FFF) commonly known Fused Deposition Modeling (FDM®) and selective laser sintering (SLS) [14, 15] are the trendiest techniques being used. Nowadays, these techniques are showing higher potential for product

✉ S. Terekhina
svetlana.terekhina@ensam.eu

T. Tarasova
t.tarasova@stankin.ru

S. Egorov
s.egorov@stankin.ru

L. Guillaumat
Laurent.Guillaumat@ensam.eu

M. L. Hattali
lamine.hattali@universite-paris-saclay.fr

[1] Arts et Métiers ParisTech, Campus Angers - Laboratory LAMPA - 2 Bd du Ronceray, 49035 Angers Cedex 1, France

[2] Moscow State University of Technology "STANKIN", 3-A Vadkovskiy Pereulok, Moscow 127055, Russia

[3] Université Paris-Saclay, CNRS, FAST, 91405 Orsay, France

manufacturing, with the capability of competing with conventional polymer-processing techniques. The FFF process consists of heating a thermoplastic material slightly above its melting point inside a nozzle. The viscous material is then extruded out of a nozzle, deposited sequentially, and additively, according to the corresponding G-code, to manufacture objects described by the standard tessellation language (.STL file) [2, 16]. This is a less aggressive process compared to injection molding where the plastic is melted and uniformly blended using a screw extruder to inject the material at high pressure into a mold. The SLS is a layer-by-layer production by sintering powdered materials using infrared laser beams. This process starts with a powder bed of polymer powder of a specific layer height and temperature. A high-powered laser is rastered across the surface to locally heat the polymer powder [14, 15]. For both processes, the performance characteristics of parts vary widely. For an accurate prediction of the behavior of parts in the given conditions, they are subjected to preliminary tests. In addition to quasi-static tests and dimensional accuracy, which are widely reflected in the literature [17–21], fatigue tests are necessary, giving the most complete picture of the material behavior under life service. According to various bibliographic sources, specimens of polymers undergo fatigue bending, tension-tension fatigue, and others [2, 22]. Polyamides (PA), acrylonitrile butadiene styrene (ABS), polylactide (PLA), and several other neat, filled and reinforced plastics are among polymers under study [23–27]. Different variable parameters associated with each type of printing technique affect the mechanical characterization of the specimens. Several studies have reported some parameters which could potentially affect mechanical properties and fatigue life of 3D-printed parts [28–39]. We note that the most important parameters for the FFF process are (i) layer height, (ii) layer thickness, (iii) raster orientation, (iv) extruder temperature, (v) gap between raster, (vi) feed rate, and (vii) build orientation, whereas in the SLS, these are (i) energy input, (ii) preheating temperature, (iii) scan speed, (iv) scan spacing, and (v) layer thickness. Several works have been done on the mechanical behavior of additive manufactured parts, both on SLS and FFF. Some works compare these processes with the results of tests of cast specimens [40, 41]. However, to our knowledge, no research has addressed the comparison of FFF and SLS technologies among themselves on the fatigue characteristics of the obtained specimens.

This research aims to evaluate which of the two SLS or FFF processes, with a set of parameters chosen in this article, corresponds better to the fatigue resistance. In our analysis, we discuss, in every case, how the obtained degree of crystallinity, porosity, and roughness affects fatigue behavior. Our results are compared to the conventional manufacturing process methods, such as extrusion and injection molding, to see whether or not it might be suitable for industrial applications.

2 Materials and manufacturing processes

2.1 Materials

Two commercially available polyamides 12 (PA12) were used in the study: (i) thermoplastic filaments STYX-12™ produced by Formfutura (Netherlands) used for the FFF process, and (ii) thermoplastic powder PA2200, supplied by EOS GmbH (Germany) used for the SLS process.

Based on polyamide PA12, the STYX-12™ is an industrial nylon filament that combines excellent mechanical, chemical, and hygroscopic properties with printability. The STYX-12™ has a very low water absorption compared to other nylons. This combination of properties has resulted in high-performance and industrial-grade nylon which can be printed on a wide range of FFF/FDM 3D printers. However, it is recommended to dry the material before each printing. In that case, the filament was carried out at 60 °C in a vacuum oven for 6 h. This time is required to stabilize the weight loss of the filament.

The PA2200 is a mixture of 40% new and 60% one-time-recycled industrial-grade powder material that exhibits high strength and stiffness, good chemical and long-term stability, and high detail resolution. Their important properties are connected with human body interaction. It manifests biocompatibility so it can be used within the human body. In compliance with the EU Plastics Directive 2002/72/EC, it can also be used for food contact [42–44]. The material properties of given polymers are summarized in Table 1.

To note that, in general, the mechanical and fatigue properties of the nylon were negatively related to their moisture content: it reduces strength, stiffness, and natural frequency, while increasing energy absorption and ductility in the material. The moisture in nylon acts as a plasticizer that reduces the entanglement and bonding between molecules, therefore increasing their volume and mobility and thus decreasing the glass transition temperature (Tg), which makes nylon easier for further crystallization. Practically, the best way to minimize the moisture uptake is to select plastics with a low absorption rate (as in our case for PA12) or design products in ways that prevent excessive absorption. In this context, all the produced specimens were stored in the dry atmosphere of a desiccator prior to testing.

2.2 Manufacturing processes

The SLS process was conducted on the EOS Formiga P100 machine (EOS GmbH Electro Optical Systems, Krailling, Germany). There is an important number of parameters that significantly influence the geometry and mechanical properties of the obtained specimens. Some of them are controllable, such as laser energy density, location in the chamber, layer thickness, chamber temperatures, orientation of the specimens

Table 1 Material properties of PA12 polymers given by the manufacturer

Material	PA12 (PA2200, SLS)	PA12 (STYX-12™, FFF)
Chemical formula	$[–NH–(CH_2)_{11}–CO–]_n$	
Grain size (μm)/diameter (mm)	56	1.75
Melting temperature: T_m (°C)	172-180	250 ± 10
Tensile modulus when 3D printed (MPa)	1700	1400
Tensile strength when 3D printed (MPa)	48	60
Coefficient of thermal expansion ($\times 10^{-6}$ K^{-1})	109	100
Water absorption (% weight increase, saturated)	1.33	1.6
Density (g/cm^3)	0.45	1.02

in the building envelope, scanning strategy, and velocity, while other factors, such as temperature gradients in powder and contraction at cooling, can be considered noise. Therefore, the decision to take these and not other parameters are difficult. Based on a set of mechanical tests conducted, the optimum process parameters are mentioned in Table 2. Rectangular bending specimens, according to the ISO 178:2010 [45], were printed on-edge (*XZ* plane) build orientations with PA2200 powder (see Fig. 1b).

The specimens of the FFF process were manufactured on the open-source Spiderbot 3D printer (Fig. 2a). A software, Simplify3D version 4.1, was used for slicing the .STL files into machine-readable g-code. Rectangular specimens intended for standard quasi-static flexural and fatigue mechanical analysis were directly fabricated, the dimension of which is $100 \times 20 \times 4$ mm^3. Figure 2b shows the STL file of the bending test specimen conforming to the ISO 178: 2010 [45]. It is well known that the part build orientation and raster orientation are parameters with great influence on the mechanical properties of the printed material. They present a synergetic interaction between them, i.e., the part build orientation modifies the raster orientation. Consequently, for simplification reason, all specimens were printed with the raster orientation of 0°, i.e., unidirectional (see Fig. 2b). After conducting many experimental trial runs and based on our published data and literature review [46, 47], we have chosen to print the part in *XZ* plane build orientation (on-edge), which presents the best mechanical properties compared to *XY* (flat) and *YZ* (upright) plane build orientations.

Table 3 summarizes the important printing parameters used in the FFF process.

Table 2 Fixed SLS process parameters used to print PA12 specimens

	SLS printing parameters of PA12
Laser power, W	30
Layer thickness, mm	0.1
Laser velocity, mm/s	1500
Scan spacing, mm	0.25
Laser beam diameter, mm	0.29
Building chamber temperature, °C	171
Removal chamber temperature, °C	150
Sintering temperature, °C	185
Preheating time, h	3

3 Experimental procedure

Before testing, the melting temperature and crystal weight fraction X_c of PA12 were measured by using differential scanning calorimetry (DSC) (DSC 404 F1). All specimen dimensions were measured by a set of digital Vernier calipers, and their surface roughness was scanned by a Bruker mechanical Profilometer (Dektak-XT). Specimen densities were calculated based on Archimedes' principle, and 2D porosity size and morphology were analyzed through the ImageJ 1.53a software. These data were used to ensure that all test specimens were in similar conditions and for interpretation results.

3.1 DSC

The thermal properties of PA12 polymers were analyzed by differential scanning calorimetry (DSC) on a DSC404 F1 machine (Netzsch, German). Test specimen fragments (length and width ~ 1 mm, thickness ~ 200 μm) were carefully cut by scissors from the bottom supportive layer of specimens used in quasi-static mechanical tests. Each sample weighed 8–10 mg. A heating/cooling rate **k** of 10 °C/min from 25 to 350 °C in argon atmosphere was chosen according to ASTM D3418 [48]. This data was used to generate a graph of the heat flux versus temperature. Three specimens were tested. The melting temperature (T_m) and crystal weight fraction (X_c) of the specimen were measured after the additive process. The X_c was determined by

$$Xc = \frac{(\Delta H_m - \Delta H_{cc})}{\Delta H_{m_0}} \quad (1)$$

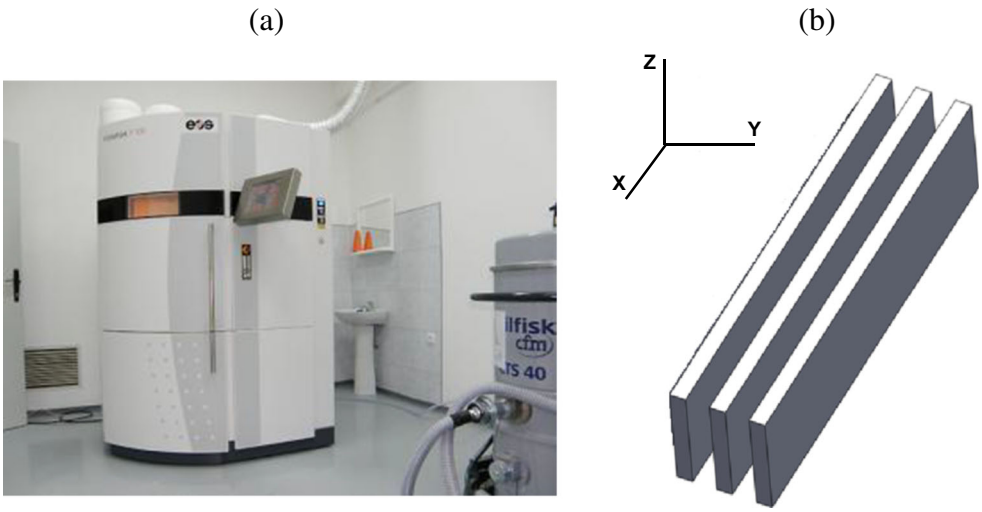

Fig. 1 **a** SLS printer: EOS FORMIGA P100; **b** rectangular bending specimens, according to the ISO 178:2010 printed on-edge (XZ plane) build orientation with PA2200 powder

where ΔH_m is the area under the melting endotherm, ΔH_{cc} is the area under the cold crystallization/recrystallization curve, and ΔH_{m_0} is the heat of fusion for 100% crystalline sample (245 J/g for PA12 [49]).

3.2 Determination of porosity

Density is obtained by weighing the cut PA12 specimens before and after impregnation with diiodomethane (CH_2I_2) [50] and determination of their volume from the Archimedes force:

$$\rho = \frac{m_a}{m_{a(CH_2I_2)} - m_{H_2O(CH_2I_2)}} \rho_{(H_2O)} \quad (2)$$

where m_a, $m_{a(CH_2\ I_2)}$, and $m_{H_2O(CH_2\ I_2)}$ are the specimens weighed in air, diiodomethane, and water with diiodomethane respectively; $\rho_{(H_2O)}$ is the density of water. Note that the impregnation with diiodomethane, which is a compound immiscible with water, prevents water from penetrating the open pores of the specimens. Thus, the truly measured porosity is expressed by

$$\text{Porosity} = \left(1 - \frac{\rho}{\rho_s}\right) 100 \quad (3)$$

where ρ_s is the density of the initial material ($\rho_{PA12\ FFF} = 1.02$, $\rho_{PA12\ SLS} = 0.45$).

3.3 Analysis of porosity

The pictures of the cross-section and lengthwise-section specimens were imported into ImageJ 1.53a, and the surface area of the pores was measured through the Analyze Particles option. The first step consisted of using thresholding. Raw images were converted to binary images (Fig. 3), in which the object pixels are white and the pixels representing the pores are black.

Then, the Analyze Particles option was applied (Fig. 3). This command counts and measures objects in thresholded images. It then outlines the object using the wand tool, measures it using the Measure command, fills it to make it invisible, and then resumes scanning until it reaches the end of the image or selection.

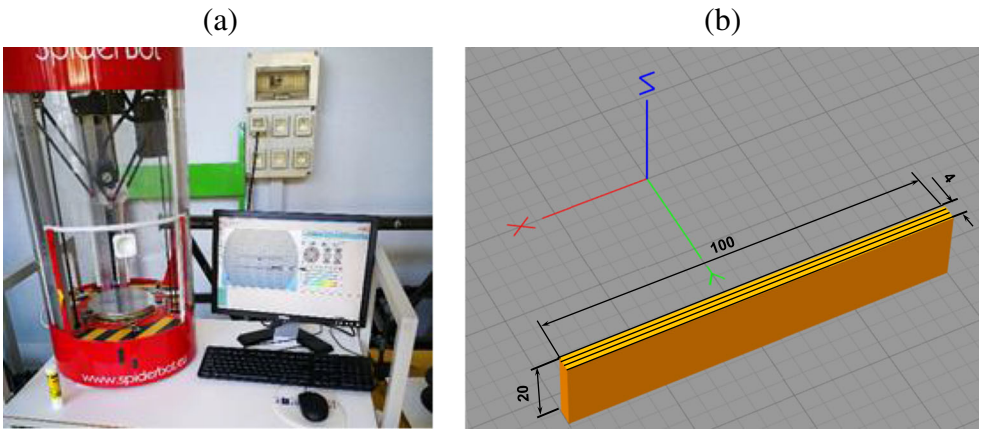

Fig. 2 **a** FFF open-source Spiderbot 3D printer; **b** printing direction configuration for the FFF process, using Simplify3D

Table 3 Fixed FFF process parameters along with their nominal values

	Printing parameters of PA12
Color filament	Colorless
Print speed, mm/min	1900
Movement speed, mm/min	5400
T_{bed}, °C	100
T_{head}, °C	245
Extrusion width	0.67
Layer height, mm	0.2
Nozzle diameter, mm	0.5
Extrusion multiplier	1
Overlap, %	40
Number of contours	3
Infill percentage, %	100
Raster orientation, °	0

3.4 Roughness characterization

The roughness surface of studied specimens was analyzed by a Bruker mechanical Profilometer (Dektak-XT). 3D topography profiles are recorded. Forty profiles are scanned along the x-direction. Their length is 2 mm. Each profile has been positioned in the central part of the specimen and on the top surface opposite the bed printer.

3.5 Mechanical characterization

3.5.1 Quasi-static flexural tests

Quasi-static flexural mechanical property tests were conducted in the three-point-bending mode according to the ISO 178:2010 [45]. The tests were carried out to establish an elastic flexural modulus (E_f), an elastic limit stress ($\sigma_{el.f}$), and an ultimate flexural strength ($\sigma_{ult.f}$) (Fig. 4a).

The distance between the two support pins was L = 80 mm. The ratio L/h was equal to 20, which allows ignoring the shear stresses during testing. The tests were carried out on an electro-mechanical testing machine (Zwick) under the displacement-controlled condition at a constant rate of 100 mm/min (Fig. 4b). At least five specimens were tested.

3.5.2 Fatigue flexural tests

Three-point bending cyclic tests were performed on an in-house built flexural fatigue test machine designed at the LAMPA laboratory (Fig. 5). The same specimen dimensions and span length as for the quasi-static testing were used. The fatigue tests were displacement-controlled with various strain ratios r defined by

$$r = \frac{\varepsilon_{max}}{\varepsilon_{el}} \tag{4}$$

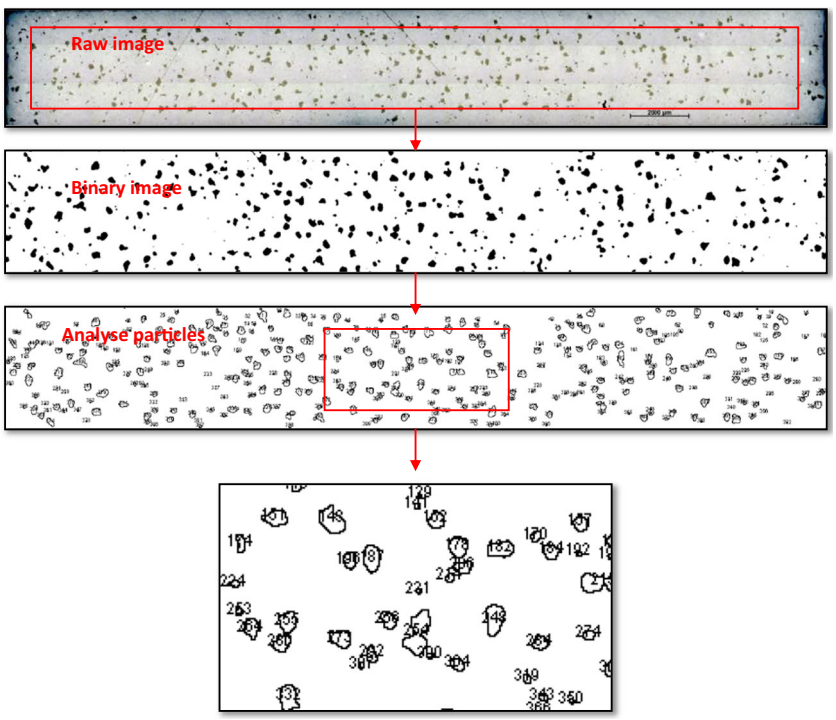

Fig. 3 Analysis of pore size by the Analyze Particles option in ImageJ

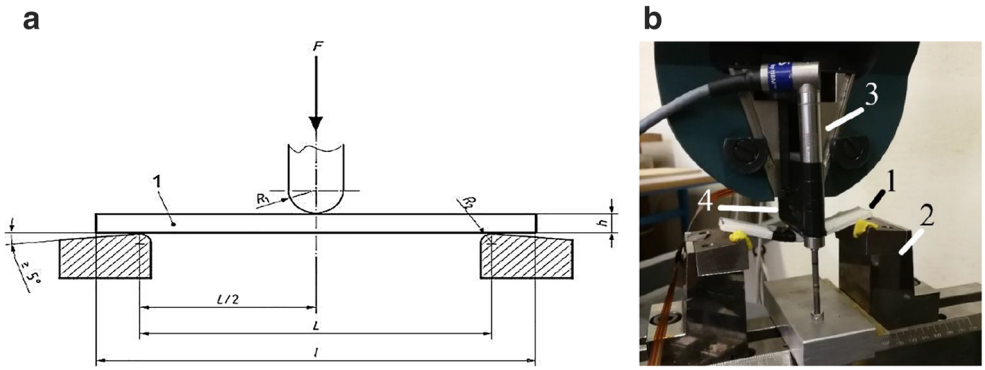

Fig. 4 **a** According to the ISO 178:2010 standard, the sample dimensions for three-point bending testing were defined as R_1 = 5 mm, R_2, = 2.5 mm, L = 80 mm, h = 4 mm, and l = 100 mm and **b** Zwick testing machine: 1—specimen, 2—support, 3—displacement sensor, and 4—punch

with ε_{max} and ε_{el} , respectively, the maximal strain applied during the fatigue tests and the average elastic strain measured during quasi-static tests. Note that to have maximum reduction of the visco-plastic behavior of materials during the fatigue tests, all the specimens tested were conducted in their visco-elastic domain.

Since there is currently no material standard for additive manufactured parts, the recommendation from a similar material standard for the flexural fatigue properties of plastics was used [51]. The tests were performed with a frequency of 5 Hz. Figure 6 shows the temperature variation at the center of the specimen as a function of cycle number for both processes at different loading ratios. It should be noted that a fast increase in temperature at the beginning of the test is followed by a stabilization corresponding to the equilibrium between the generated thermal energy as a result of the dissipative processes, called the self-heating, and the thermal energy convected and radiated to the environment. The phenomenon of self-heating refers to the internal friction (damping) of the material on a molecular level. Thus, the heat resulting from the dissipative processes causes the increase of the temperature of the loaded structure [52].

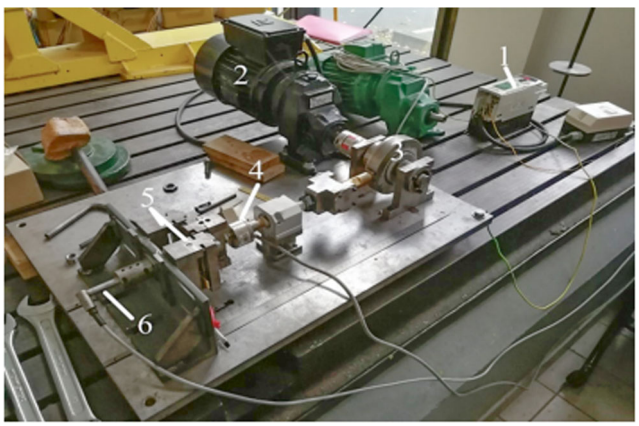

Fig. 5 Experimental set-up of fatigue test: 1—frequency controller, 2—engine, 3—eccentric, 4—load cell, 5—support, 6—displacement sensor LVDT

The temperature of the specimen was not significantly affected by this frequency; the observed change in temperature was much smaller than the recommended maximum temperature rise of 10 °C for all applied ratios *r* [53] (see Fig. 6). The tolerable threshold was taken as a temperature rise less than 10 °C relative to ambient conditions.

At least three specimens per loading configuration were tested. The experimental program is summarized in Table 4.

4 Results and discussion

4.1 Microstructure characterization

4.1.1 DSC

DSC is a technique used to study the behavior of polymers when they are heated and/or cooled. It can provide valuable information about the thermal transitions, crystalline melting enthalpies, cold crystallization/recrystallization, and degree of crystallinity of a material corresponding to its behavior during the process. The properties of plastics are significantly influenced by their degree of crystallinity (X_c). The higher the X_c, the stiffer and stronger, but also more brittle, a printed part is.

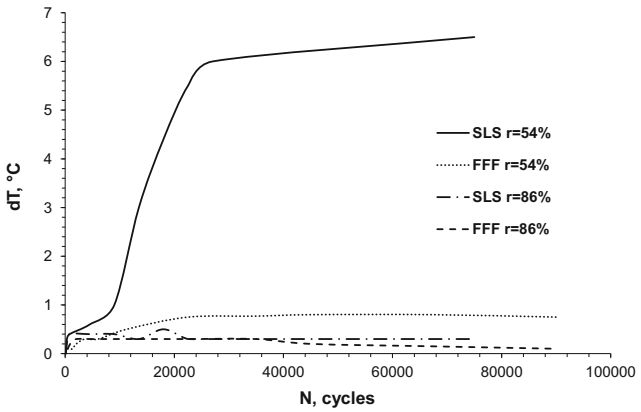

Fig. 6 Temperature evolution of the central part of the specimen measured by a thermocouple at several loading ratios

Table 4 Experimental conditions for fatigue tests

Material					
PA12 (FFF/SLS)	ε_{max}, %	0.9	1.5	2.1	2.4
	r, %	32	54	75	86
	No. of specimens tested	3	3	3	3

Table 5 Average values of 3 DSC analyses

Process	T_g, °C	ΔH_m, J/g	ΔH_{cc}, J/g	X_c, %	T_m, °C
FFF	132 ± 1	25 ± 0.2	13.8 ± 0.2	5 ± 0.5	253 ± 1.2
SLS	53 ± 2	56 ± 0.4	–	23 ± 0.1	190 ± 3.5

Therefore, to understand and compare both studied processes, it is necessary to know the thermal properties of PA12 specimens.

Figure 7a, b show a DSC graph of heat flux (mW/mg) versus temperature (°C) for studied specimens.

The spectrums show a typical melting endotherm permitting to obtain and calculate the melting temperature T_m and crystal weight fraction (X_c). Indeed, the printed specimens show clear evidence of cold crystallization (at ~ 180 °C), a process associated to crystallization of the amorphous segments in the polymer above the glass transition temperature (Fig. 7a). It could be supposed that the FFF filament was quenched by the manufacturer to facilize the FFF printing process. Table 5 summarizes the obtained results that reveal the degree of crystallinity of the SLS specimens to be more than four times higher than that of the FFF ones. Only 5% of crystallinity is obtained in the latter.

In addition, the melting temperature was 253 °C and 190 °C for the FFF and SLS processes respectively. Note that Fig. 7b shows a limitation of DSC analysis concerning the glass transition temperature (T_g) determination. The latter is not clearly seen in the DSC curve if the polymer has a large crystalline region, as in this case.

4.1.2 Porosity

In addition to the intrinsic weakness originating from the layer-by-layer structure, porosity is a major concern when it comes to both SLS and FFF printed parts. Both printed PA12 specimens possessed quite a high level of porosity, the biggest size of which was hundreds of microns. The average porosity and density of PA12 are summarized in Table 6.

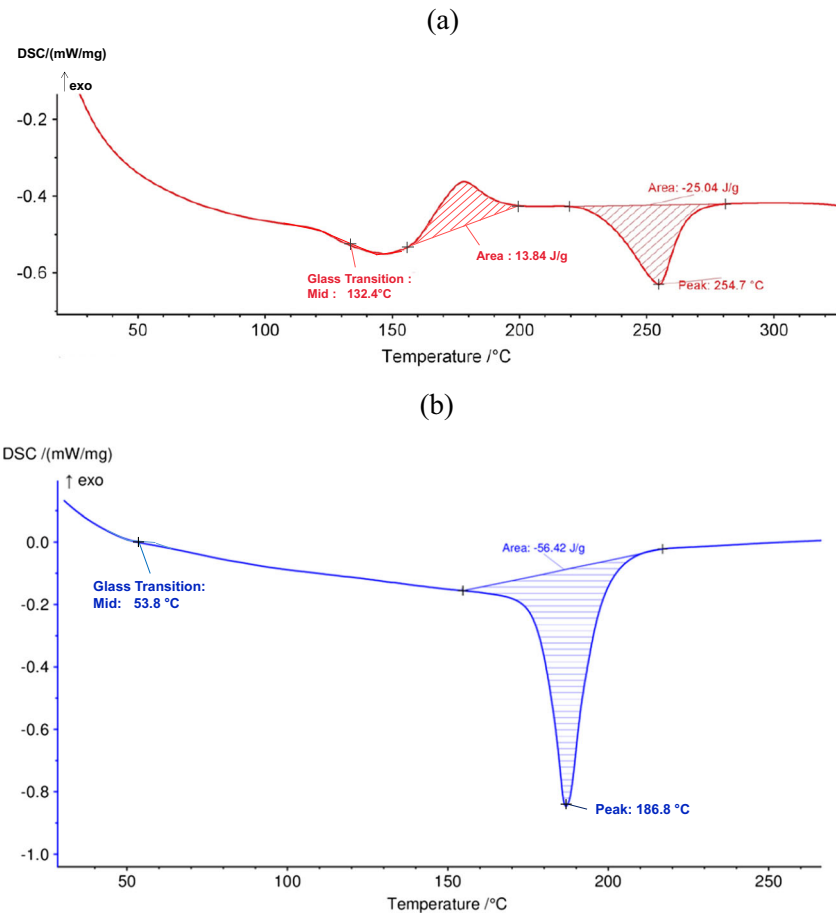

Fig. 7 An example of typical DSC data for PA12 material after **a** FFF process and **b** SLS process

Table 6 Average porosity and density of specimens for both processes

	FFF process	SLS process
Porosity (%)	10.6 ± 1.7	11.8 ± 1.8
Density (g/cm^3)	0.9032 ± 0.04	0.8905 ± 0.07

The obtained results show that the porosity seems to depend on the process. The porosity of FFF specimens is 10% less than obtained by SLS. To evaluate the porosity size of the specimen, statistical analysis was carried out. Therefore, the carefully polished cross-section observations realized on optical microscopy (Carl Zeiss Imager.M2m) are analyzed by ImageJ 1.53a. The experimental result is fitted by a Gaussian function (normal distribution) to find modal pore sizes. For SLS specimens, the statistics of the pores show that the porosity size varies between ~ 12 and ~ 250 μm with two populations of an average size of ~ 33 μm, and ~ 143 μm (Fig. 8a). This distribution indicates heterogeneity of porosity size within a specimen. As shown, there are few pores whose sizes are over 225 μm. High porosity (11.8%; see Table 6) and porosity size (> 100 μm) suggest that the laser power (LP) parameter applied in our study is high (LP = 30 W; see Table 2). Caulfield et al. [54] reported that in the case of polyamide, if the laser power increased beyond 15 W, the surface quality seemed to deteriorate giving an increasingly rougher texture and a porosity with a diameter of > 100 μm, whereas for the FFF specimen, it shows that the porosity size varies between ~ 15 and ~ 170 μm with an average size of ~ 52 μm (Fig. 8b).

4.1.3 Roughness characterization

The obtained results of roughness Ra and the 3D topography profiles are shown in Fig. 9. The results show that roughness (Ra) depended on the process. The Ra obtained on the FFF process is 43% rougher than that of the SLS process. This could be explained by the circular form of the filament that appeared on the surface.

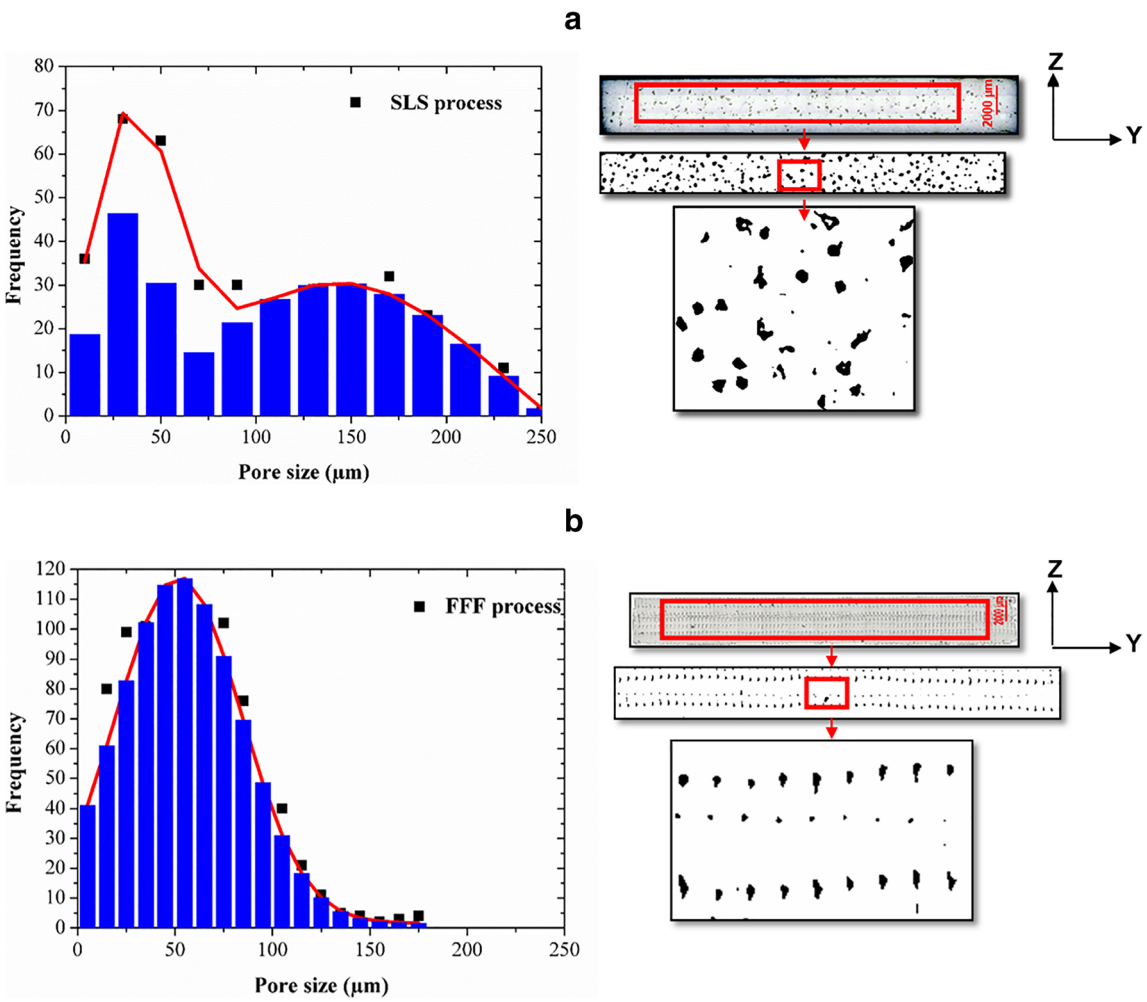

Fig. 8 Cross-section pore size distributions for **a** SLS and **b** FFF processes. Each data was fitted using a Gaussian distribution to find modal pore sizes

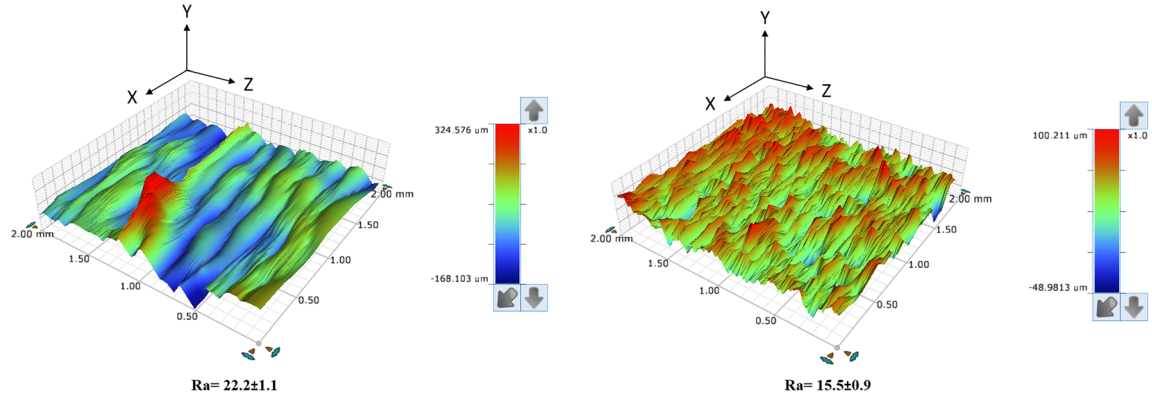

Fig. 9 3D topography profiles of specimen printing by **a** FFF process and **b** SLS process. Ra (μm) is the arithmetic mean surface roughness; it is by far the most commonly used parameter in surface finish measurement and for general quality control

4.2 Influence of processes on quasi-static flexural behavior

The plot of average stress against an average strain of five specimens of each process is shown in Fig. 10. As can be seen, the mechanical properties of both processes are close. The averages of both elastic limit stress ($\sigma_{el.f}$) and maximum bending stress ($\sigma_{ult.f}$) associated with the FFF process are approximately 3.2 MPa (or ~8%) and 2 MPa (or ~3%) greater than the SLS process respectively. The reason that can explain this behavior is related probably to the porosity content in specimens obtained by both processes (cf. Table 6 and Fig. 8).

However, the SLS specimens are stiffer than the FFF ones due to their higher degree of crystallinity (cf. Fig. 7). The same comparison was achieved with those of conventional manufacturing processes (see Table 7). The flexural modulus of PA12 specimens obtained by SLS is ~21% and ~37% better than that of the PA12 manufactured by IM and extruded processes respectively. It is also ~6.5% and ~25% better for FFF specimens. Besides, flexural maximum stresses are similar to those obtained by IM and extrusion techniques.

Note that all studied specimens were not failed after a significant deflection (more than 10% strain) and, thus, are considered as "ductile." Satisfactory repeatability is achieved for all performed tests, with bending property scattering that does not exceed 10%.

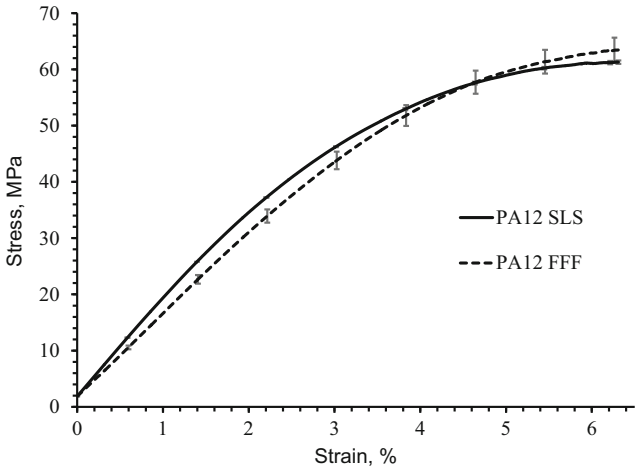

Fig. 10 Comparison of average stresses versus average strain of PA12 specimens manufactured by SLS and FFF respectively

4.3 Influence of processes on fatigue properties

4.3.1 Fatigue behavior

The evolution of the mechanical properties of PA12 with the number of cycles was studied in its visco-elastic domain. Figure 11 shows the average evolutions of the maximum load F_{max} applied, with the number of cycles, normalized by the initial maximum load F_{max0} for different loading ratios. For the FFF specimens loading at $r = 54\%$, the evolution of stiffness is stable at first and then starts to decrease constantly until ~4%, whereas at $r = 75\%$ and $r = 86\%$, it decreases continually during the overall fatigue life until ~8% probably due to the appearance of the damage mechanisms.

Table 7 Summary of quasi-static flexural test results compared with those of conventional manufacturing processes

Material/process	E_f, MPa	$\sigma_{el.f}$, MPa	$\sigma_{ult.f}$, MPa	$\varepsilon_{el,\ \%}$	Ref.
PA12/IM	1748 ± 9	38.5 ± 0.2	61 ± 0.3	2.8	
PA12/IM	1472 ± 51	41.7 ± 1.4	63 ± 2	2.8	
PA12/IM	1376	–	61	–	[55]
PA12/extrusion	1300	10–56	56	–	[56]
	900–1200	50	50–65	–	[57]

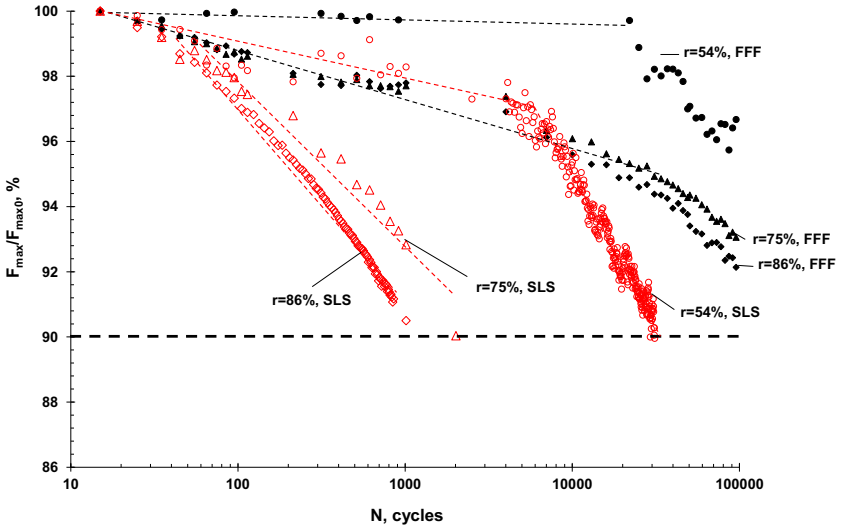

Fig. 11 Evolution of the normalized average maximal load applied versus the number of cycles for FFF and SLS specimens

For the SLS specimens loading at $r = 54\%$, this corresponds to slow stiffness degradation during the first 10^4 cycles, followed by a rapid decrease, whereas at $r = 75\%$ and $r = 86\%$, the stiffness degradation starts to decrease since the early cycles (~ 50 cycles). This is could be explained by the progressive evolution of the damage mechanisms. The latter is expressed by a semi-logarithmic quasi-linear law:

$$F_{max}/F_{max0} = 1 - B \log_{10}(N) \quad (5)$$

where B is the slope that represented the degradation rate ($1/N$) and N is the number of cycles.

In theory, stiffness degradation in the FFF process results from crack propagation and/or degradation of filament deposited. In our case, the optical micrograph of the lengthwise section of the specimens loading at $r = 86\%$ shows that the slight degradation mechanism observed is attributed solely to the growth of micro-delamination fatigue cracks at the interface between layers at the level of the load applied (Fig. 12a, b).

For the SLS process, the bimodal statistics of the pores after the process and fatigue loading at $r = 86\%$ showed that the porosity size varies between an average size of ~ 39 μm and

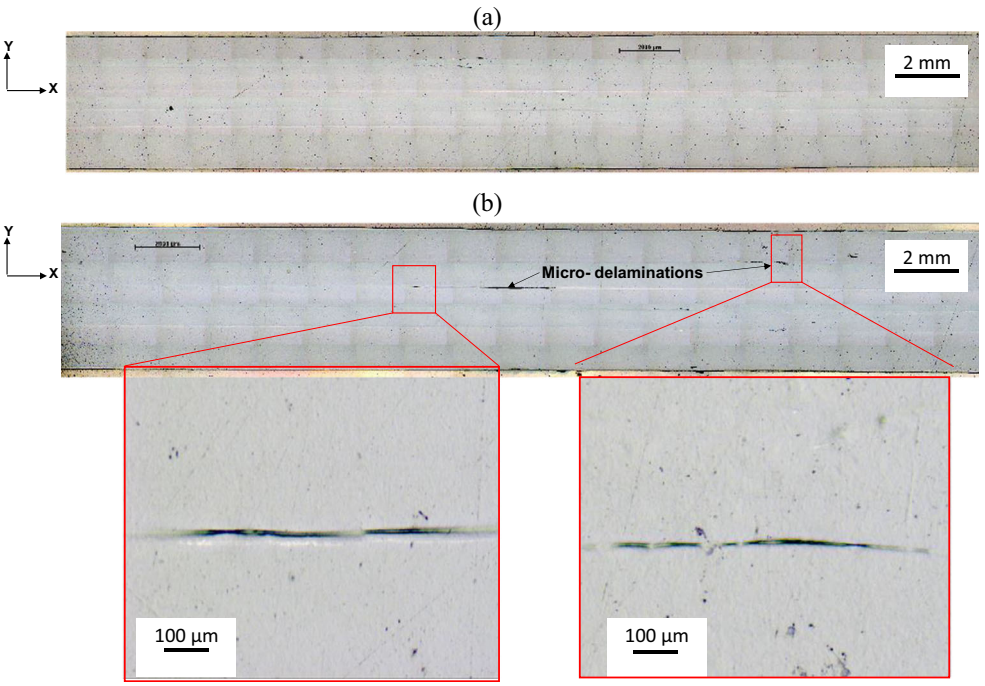

Fig. 12 Micrograph of the lengthwise section distribution of PA12 specimens: **a** after the FFF process, **b** after the fatigue test at $r = 86\%$

~148 μm to ~55 μm and ~172 μm respectively, and suggested that the degradation mechanism occurred by pore growth (Fig. 13a–d). Pores in PA12 specimens act as stress concentrators that encourage localized damage and can be sources of crack initiation and propagation. The stress concentration factor varied significantly with the pore location. Li [58] indicated that the stress/strain concentrations reached their peaks when a pore of 200 μm in diameter was just buried beneath the surface, as it was in our case.

The endurance diagram was plotted to determine the end of life according to an N_{10} criterion for different loading ratios r (Fig. 14a). This criterion is satisfied when a 10% decrease in the maximum applied load is observed. It was chosen because, under three-point-bending fatigue with imposed displacement, a breakage of the PA12 specimens has never been observed. Besides, 3D printing creates anisotropic specimens, as in the case of composites, and, therefore, the large dispersion at the end of life.

The fatigue properties of PA12 obtained by FFF have never reached the N_{10} criterion at loading ratios applied contrary to SLS specimens. Although the PA12 material obtained by the SLS process is more crystalline when compared to PA12 obtained by FFF, the latter has a higher overall fatigue life. However, the operating range of the fatigue machine did not allow a detailed conclusion about its fatigue properties. Lesser [59] also observed a higher overall fatigue life of polyamide compared to polyacetal despite a higher degree of crystallinity of the latter. Based on this data, a simple linear model of the fatigue properties for the SLS specimens has been developed, using the least-squares method. The function of the linear model follows the form of Eq. (5) coupled with the N_{10} criterion. The linear model plotted in Fig. 14a for the SLS is shown in Eq. (6):

$$r = 1.4742 - 0.092 \log_{10}(N_{10}), \text{with } R^2 = 0.9297 \quad (6)$$

The R-square value of the normalized model was greater than 0.92. This means that 92% of the response variance is accounted for by the linear model.

The value $|1/B|$ was thus used to compare the fatigue properties of the studied material and processes to those of PA12 obtained by conventional processes [60–62]. In fact, the materials with ratio $|1/B|$ are the highest present longer the end-of-life and smaller degradation rate. The value $|1/B|$ of pseudo-Wohler's curves of studied processes was thus considered. The end-of-life properties in fatigue of PA12 obtained by injection molding and extrusion are presented in Table 8. Figure 14b presents this comparison. The $|1/B|$ ratio is the smallest for laser-sintered PA12 and is 24% and 40% less than IM and extruded specimens respectively.

4.3.2 Energy analysis

Quantitative characterizations of the hysteresis cycles of PA12 were conducted. Each of the stored hysteresis loops (Fig. 15)

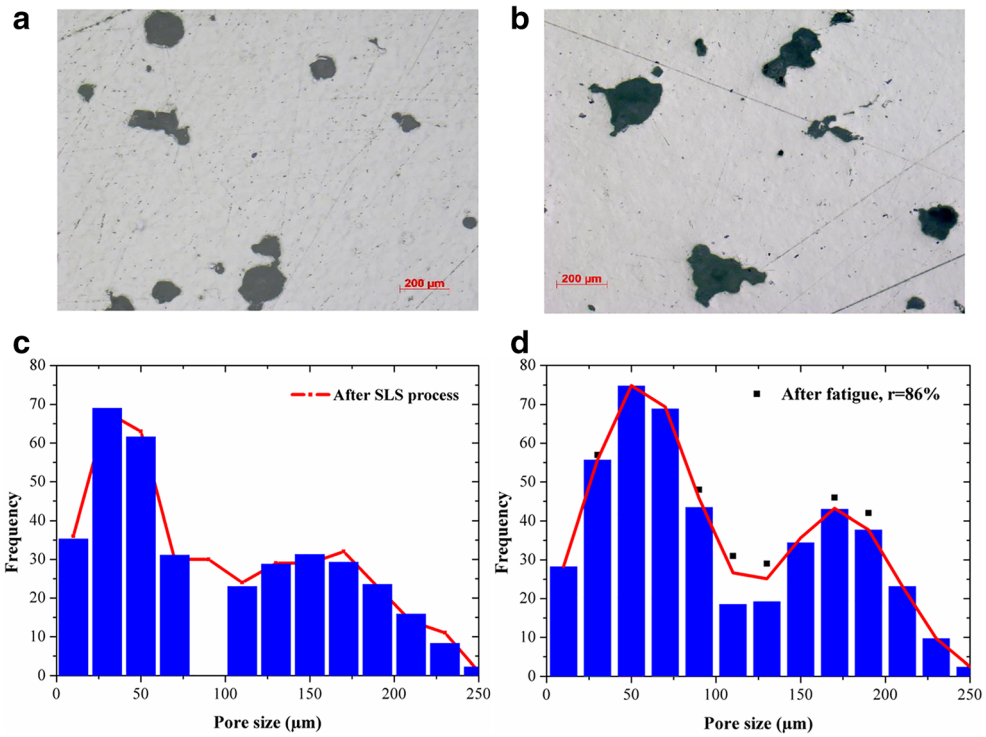

Fig. 13 Micrograph of the lengthwise section and pore size distribution of PA12 specimens: **a**–**c** after the SLS process, **b**–**d** after the fatigue test at $r = 86\%$

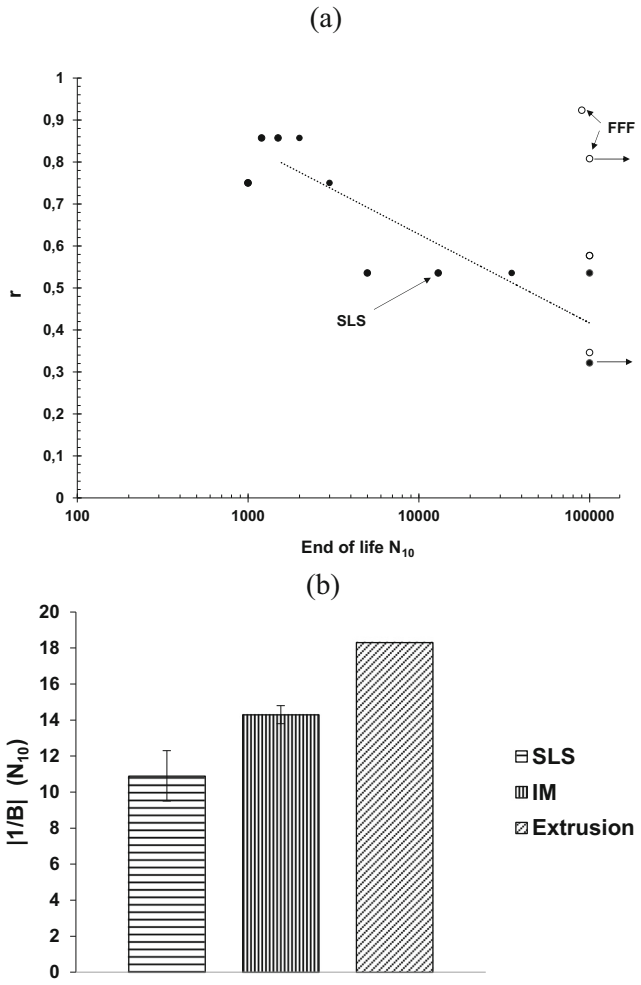

Fig. 14 **a** Endurance diagram for PA12 material for two considered processes; **b** fatigue performances of the studied polymer compared to other polyamide materials obtained by the conventional process

were digitally processed with a MATLAB® designed to calculate:

- The maximum potential energy E_p, corresponding to the total area under the force-displacement curve related to the loading phase of the hysteresis cycle, and expressed as

$$E_p = \frac{1}{2}\sum_{i=1}^{n}(d_{i+1}-d_i)\left(f\left(d_{i+1}\right)+f(d_i)\right) \quad (7)$$

Table 8 End-of-life properties in fatigue of PA12

Material	PA12		
Manufacturing method	SLS	IM [60, 61]	Extrusion [62]
Fatigue test mode	3-point flexure, $f = 5$ Hz	Tension-compression, $f = 3$ Hz	Flexure, $f = 10$ Hz
$\|1/B\|$, (N_{10})	10.9 ± 1.4	14.28 ± 0.5	18.3

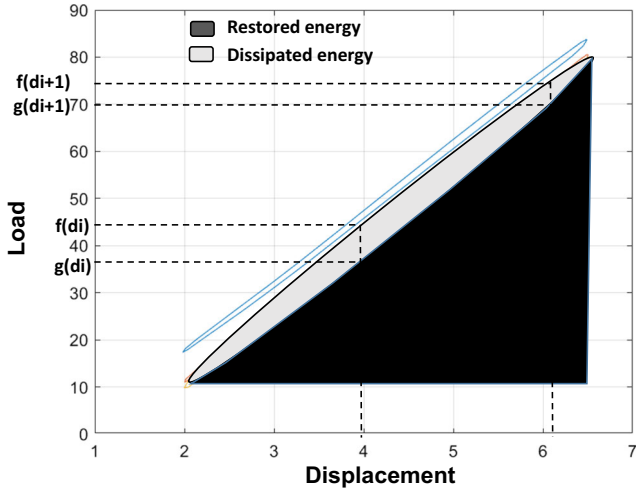

Fig. 15 Illustration of hysteresis cycles (in blue—the first cycle and in gray—the last cycle) and its main parameters in the fatigue test

- The elastic energy E_r that is given by the area under the curve corresponding to the unloading phase which is calculated by

$$E_r = \frac{1}{2}\sum_{i=1}^{n}(d_{i+1}-d_i)\left(g\left(d_{i+1}\right)+g(d_i)\right) \quad (8)$$

- The energy dissipated by the material E_d and corresponding to the area of the hysteresis cycle which is given by

$$E_d = \frac{1}{2}\sum_{i=1}^{n}(d_{i+1}-d_i)\left(\left(f\left(d_i\right)+f(d_i)\right)-(g(d_{i+1}+g(d_i))\right) \quad (9)$$

- And the loss factor η defined as the ratio of the energy dissipated to the potential energy and given by

$$\eta = \frac{E_d}{2\pi E_p} \quad (10)$$

Figure 16 presents the evolution of the average fatigue loss factor η for polymer tested after FFF and SLS, and for different loading ratios r.

The small values of loss factor (less than 0.015) were obtained for both considered processes. This is due to the quasi-absence of the dissipative effect of the polymer during the fatigue. However, in more detail, the loss factor is relatively stable at first and then increases slightly and continually at the end of the fatigue test that is also considered as the sign of visco-elastic dissipation and slight heating of polymer [63].

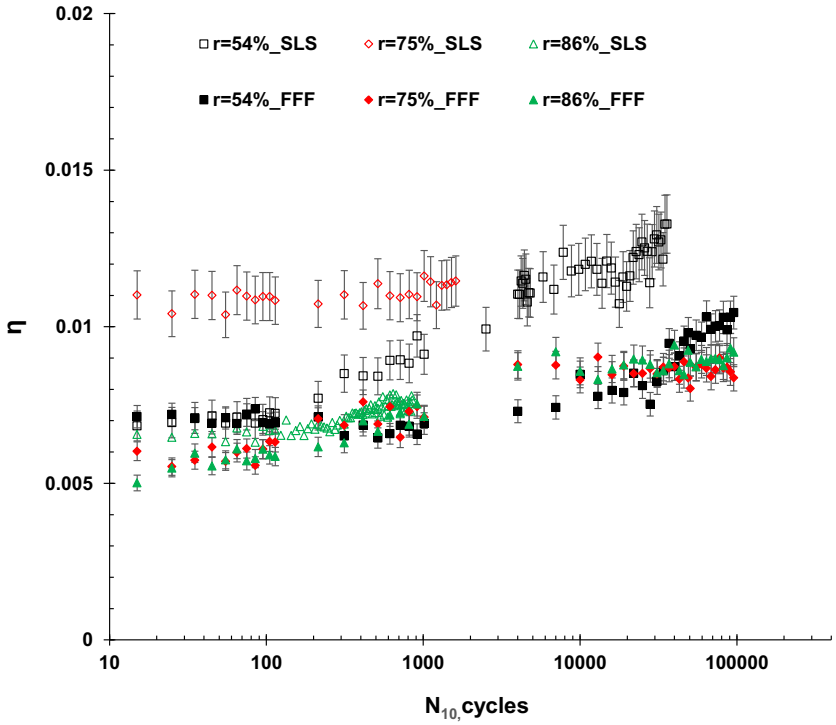

Fig. 16 The evolution of the loss factor with the number of cycles corresponded to 10% of loss stiffness and for different loading ratios for PA12 after FFF and SLS processes

5 Conclusions

This work focused on the experimental analysis of the quasi-static and cyclic flexural properties of PA12 obtained by FFF and SLS. The following conclusions could be drawn:

1. Naturally, the mechanical and fatigue properties of the 3D-printed polymer specimens can vary according to not only their porosity and pore characteristics but also their surface roughness and degree of crystallinity. In our case, the SLS specimens of PA12 are about 16% flexural stiffer than the FFF ones due to their more than four times higher degree of crystallinity. However, they have similar elastic bending limit stress ($\sigma_{el.f}$) and maximum bending stress ($\sigma_{max.f}$), despite the difference of 10% in the porosity content in specimens obtained by both processes. As for the surface roughness, there is no evident effect on the mechanical and fatigue properties, despite high roughness (43%) of FFF specimens compared to the SLS ones.
2. The quasi-static flexural properties of PA12 obtained by FFF and SLS reveal better characteristics compared to IM and extruded specimens which is promising for the industry of additive manufacturing.
3. At lower stress levels in the visco-elastic domain and according to the N_{10} criterion of the end of life, the degradation rate of the SLS deposited PA12 is 24% and 40% smaller than IM and extrusion one because of high pore content. Besides, the principal fatigue damage of SLS specimens is due to the growth of pores with the loading ratio applied. Moreover, despite the almost amorphous state of PA12 FFF specimens, its fatigue behavior is more resistant than this one obtained by SLS in the considered testing range. Only a few micro-delaminations were observed in their cases that did not impact the fatigue performance.
4. At lower stress levels, PA12 dissipates and heats slightly at the end of the fatigue test. Further investigations need to measure indirectly the local dissipated energy by FE computations to strengthen the hysteretic analyses of polyamide material.

It is necessary to mention that the predictive model of fatigue life developed in this work was derived from microscopic observations in two dimensions (2-D). To develop a more accurate fatigue life constitutive equation involved in the interaction between fatigue damage and porosity, it is necessary to analyze the pores in three-dimensional microtomographic images. This route is under exploitation.

Acknowledgments The authors thank Pichereau Benoit and Gallegos Linamaria from Arts et Métiers ParisTech, Campus Angers, for helpful discussions and technical support.

Funding The authors disclosed receipt of the following financial support for the research, authorship, and/or publication of this article: This study was supported by the French-Russian collaboration project and financed by the Ministry of Education and Science of the Russian Federation as part of the implementation of the state task № 0707-2020-0034.

Availability of data Not applicable.

Compliance with ethical standards

Conflict of interest The authors declare that they have no conflicts of interest.

Code availability Not applicable.

References

1. Dizon JRC, Espera AH, Chen QY, Advincula RC (2018) Mechanical characterization of 3D-printed polymers. Addit Manuf 20:44–67
2. Safai L, Cuellar JS, Smit G, Zadpoor AA (2019) A review of the fatigue behavior of 3D printed polymers. Adv Manuf 28:87–97. https://doi.org/10.1016/J.ADDMA.2019.03.023
3. Melnikova R, Ehrmann A, Finsterbusch K (2014) 3D printing of textile-based structures by Fused Deposition Modelling (FDM) with different polymer materials. IOP Conf Ser Mater Sci 62
4. Bakarich SE, Gorkin R, Panhuis MIH, Spinks GM (2014) Three-dimensional printing fiber reinforced hydrogel composites. ACS Appl Mater Interfaces 6(18):15998–16006
5. Kalita SJ, Bose S, Hosick HL, Bandyopadhyay A (2003) Development of controlled porosity polymer-ceramic composite scaffolds via fused deposition modeling. Mater Sci Eng C Biol Sci 23(5):611–620
6. Melchels FPW, Feijen J, Grijpma DW (2010) A review on stereolithography and its applications in biomedical engineering. Biomaterials 31(24):6121–6130
7. Murphy SV, Atala A (2014) 3D bioprinting of tissues and organs. Nat Biotechnol 32(8):773–785
8. Rengier F, Mehndiratta A, von Tengg-Kobligk H, Zechmann CM, Unterhinninghofen R, Kauczor HU, Giesel FL (2010) 3D printing based on imaging data: review of medical applications. Int J Comput Assist Radiol Surg 5(4):335–341
9. Wu GH, Hsu SH (2016) Review: Polymeric-based 3D printing for tissue engineering. J Med Biol Eng 35(3):285–292
10. Stansbury JW, Idacavage MJ (2016) 3D printing with polymers: challenges among expanding options and opportunities. Dent Mater 32(1):54–64
11. Crivello JV, Reichmanis E (2014) Photopolymer materials and processes for advanced technologies. Chem Mater 26(1):533–548
12. Lee JY, An J, Chua CK (2017) Fundamentals and applications of 3D printing for novel materials. Appl Mater Today 7:120–133
13. Liu R, Wang Z, Sparks T, Liou F, Newkirk J (2017) Aerospace applications of laser additive manufacturing. Woodh Pub Ser Elect 88:351–371
14. Wohlers TT, Associates W (2012) Wohlers report 2012: Additive manufacturing and three-dimensional printing state of the industry annual. **Wohlers Associates**
15. Wohlers TT, Associates W. (2020) Wohlers report 2020: 3D printing and additive manufacturing state of the industry. **Wohlers Associates**
16. Mohamed OA, Masood SH, Bhowmik JL (2015) Optimization of fused deposition modeling process parameters: a review of current research and future prospects. Adv Manuf 3:42–53. https://doi.org/10.1007/s40436-014-0097-7
17. Lanzotti A, Grasso M, Staiano G, Martorelli M (2015) The impact of process parameters on mechanical properties of parts fabricated in PLA with open-source 3-D printer. Rapid Prototyp J 21:604–617
18. Quinsat Y, Lartigue C, Brown CA, Hattali L (2017) Characterization of surface topography of 3D printed parts by multi-scale analysis. IJIDeM 12(3):1007–1014. https://doi.org/10.1007/s12008-017-0433-9
19. Terekhina S, Skornyakov I, Tarasova T, Egorov S (2019) Effects of the infill density on the mechanical properties of nylon specimens made by filament fused fabrication. Technologies 7(3):57. https://doi.org/10.3390/technologies7030057
20. Luzanin O, Movrin D, Plancak M (2014) Effect of layer thickness, deposition angle, and infill on maximum flexural force in FDM-built specimens. J Technol Plast 39(1)
21. Turner BN, Scott AG (2015) A review of melt extrusion additive manufacturing processes: II. Materials, dimensional accuracy, and surface roughness. Rapid Prototyp J 21(3):250–261
22. Marimuthu K & al (2016) Bi-directional bending fatigue performance of unreinforced and carbon fiber reinforced polyamide 66 spur gears. Int J Prec Eng Manuf 17(8): 1025–1033
23. Mary T, Schwartz P (1992) Bending and torsional fatigue of nylon 66 monofilaments. J Appl Polym Sci 46(11):2023–2032
24. Hooreweder B et al (2013) On the difference in material structure and fatigue properties of nylon specimens produced by injection molding and selective laser sintering. Polym Test 32(5):972–981
25. Gomez-Gras G et al (2018) Fatigue performance of fused filament fabrication PLA specimens. Mater Des 140:278–285
26. John L, Huang A (2013) Fatigue analysis of FDM materials. J Rap Prototyp 19(4):291–299
27. Mejri M et al (2017) Fatigue life and residual strength of a short-natural-fiber-reinforced plastic vs nylon. Comp Part B: Eng 110: 429–441
28. Casavola C, Cazzato A, Moramarco V, Pappalettera G (2017) Residual stress measurement in fused deposition modelling parts. Polym Test 58:249–255
29. Ang KC, Leong KF, Chua CK, Chandrasekaran M (2006) Investigation of the mechanical properties and porosity relationships in fused deposition modelling-fabricated porous structures. Rapid Prototyp J 12(2):100–105
30. Equbal A, Sood AK, Mahapatra SS (2010) Prediction of dimensional accuracy in fused deposition modelling: a fuzzy logic approach. Int J Product Qual Manag 7(1):22–43
31. Sood AK, Ohdar RK, Mahapatra SS (2010) Parametric appraisal of mechanical property of fused deposition modelling processed parts. Mater Des 31(1):287–295
32. Sood AK, Ohdar RK, Mahapatra SS (2012) Experimental investigation and empirical modelling of FDM process for compressive strength improvement. J Adv Res 3(1):81–90
33. Letcher T, Waytashek M (2014) Material property testing of 3d-printed specimen in PLA on an entry-level 3d printer. Proc Asme Int Mech Eng Cong expos 2a
34. Afrose MF, Masood SH, Lovenitti P, Nikzad M, Sbarski I (2016) Effects of part build orientations on fatigue behaviour of FDM-processed PLA material. Prog Addit Manuf 1(1–2):21–28
35. Caulfield B, McHugh PE, Lohfeld S (2007) Dependence of mechanical properties of polyamide components on build parameters in the SLS process. J Mater Process Technol 182(1–3):477–488
36. Wegner A, Witt G (2012) Correlation of process parameters and part properties in laser sintering using response surface modeling. Phys Procedia 39:480–490
37. Negi S, Dhiman S, Sharma RK (2015) Determining the effect of sintering conditions on mechanical properties of laser sintered glass filled polyamide parts using RSM. Measurement 68:205–218
38. Tontowi AE, THC C (2001) Density prediction of crystalline polymer sintered parts at various powder bed temperatures. Rapid Prototyp J 7(3):180–184
39. Griessbach S, Lach R, Grellmann W (2010) Structure–property correlations of laser sintered nylon 12 for dynamic dye testing of plastic parts. Polym Test 29(8):1026–1030
40. Hooreweder BV, Kruth JP (2014) High cycle fatigue properties of selective laser sintered parts in polyamide 12. CIRP Ann 63(1): 241–244

41. Miller A et al (2017) Fatigue of injection molded and 3D printed polycarbonate urethane in solution. Polymer 108:121–134
42. ISO 10993-1 (2018) Biological evaluation of medical devices—part 1: evaluation and testing within a risk management process, International Organization for Standardization, Vernier, p 41
43. EOS GmbH Product Information. Available online: www.eos.info/material-p (accessed on 9 November 2018)
44. Borzan CS, Berce P, Chezan H, Sabau E, Radu SA, Ridzon M (2013) Physico-mechanical properties characterization of the parts from PA2200 manufactured by selective laser sintering technology. Acad J Manuf Eng 11:108–113
45. ISO 178:2010 (2010) Plastics – determination of flexural properties. ISO/TC 61/SC 2, Ed. Switzerland: International Standards Organization
46. Terekhina S, Tarasova T, Egorov S, Skornyakov I, Guillaumat L, Hattali ML (2020) The effect of build orientation on both flexural quasi-static and fatigue behaviours of filament deposited PA6 polymer. Int J Fatigue 140:105825
47. Gordelier TJ, Thies PR (2019) Optimising the FDM additive manufacturing process to achieve maximum tensile strength: a state-of-the-art review. Rapid Prototyp J 25(6):953–971. https://doi.org/10.1108/RPJ-07-2018-0183
48. ASTM D3418115, standard test method for transition temperatures and enthalpies of fusion and crystallization of polymers by differential scanning calorimetry. ASTM Volume 08.02 Plastics (II): D3222–D5083. **Available:** www.astm.org
49. Blaine RL (2002) Thermal applications note, s.l.: polymer heats of fusion
50. Dupin S (2012) Etude fondamentale de la transformation du polyamide 12 par frittage laser: mécanismes ohysico-chimiques et relations microstructures/propriétés. Dissertation, INSA de Lyon
51. ASTM D7774-12 (2013) Standard test method for flexural fatigue properties of plastics. D20.10.24, Ed. West Conshohocken, PA: ASTM International. [Online]. **Available:** www.astm.org
52. Katunin A (2018) Criticality of the self-heating effect in polymers and polymer matrix composites during fatigue, and their application in non-destructive testing. Polymers 11:19. https://doi.org/10.3390/polym11010019
53. Forster A M (2015) Materials testing standards for additive manufacturing of polymer materials: state of the art and standards applicability. US Department of Commerce, National Institute of Standards and Technology
54. Caulfield B, McHugh PE, Lohfeld S (2007) Dependence of mechanical properties of polyamide components on build parameters in the SLS process. J Mater Process Technol 182:477–488
55. Tuan Noraihan Azila Tuan R et al (2016) Comparison of mechanical properties for polyamide 12 composite-based biomaterials fabricated by fused filament fabrication and injection molding. AIP Conference Proceedings 1791(1), AIP Publishing
56. Efunda (2019) Polyamide. Material Properties. Datasheet. [En ligne] Available at : https://www.efunda.com/materials/polymers/properties/polymer_datasheet.cfm?MajorID=PA&MinorID=81
57. Biron M (2018) Thermoplastics and thermoplastic composites. Ss.l.:William Andrew
58. Li P, Lee PD, Maijer DM, Lindley TC (2009) Quantification of the interaction within defect populations on fatigue behavior in an aluminum alloy. Acta Mater 57(12):3539–3548
59. Lesser AJ (1995) Changes in mechanical behavior during fatigue of semicrystalline thermoplastics. J Appl Polym Sci 58(5):869–879
60. Hooreweder BV, Moens D, Boonen R, Kruth JP, Sas P (2013) On the difference in material structure and fatigue properties of nylon specimens produced by injection molding and selective laser sintering. Polym Test 32:972–981
61. Hooreweder BV, Kruth JP (2014) High cycle fatigue properties of selective laser sintered parts in polyamide 12. CIRP Ann 63(1): 241–244
62. GEHR Plastics (2019). GEHR PA12 TR Clearly the new kind of a anti-corrosion materials. Datasheet [En ligne] **Available at:** https://www.alro.com/datapdf/plastics/plasticsbrochures/brochure_gehrpa12_tr.pdf
63. Seignobos EM (2009) Compréhension des mécanismes physiques de fatigue dans le polyamide vierge et renforcé de fibres de verre. Dissertation, INSA de Lyon